Supplementary Information for

Nanostructure-engineered telecom quantum platform with room-temperature optical quantum coherence

Alex Kaloyeros, Natasha Tabassum, and Spyros Gallis
Corresponding author: sgalis@albany.edu

Solid-state qubit technologies

Supplemental data Table S1 provides a summary of representative near-infrared and telecom-band solid-state single-photon emitter and qubit platforms (1000 nm – 1600 nm), benchmarked across key figures of merit relevant to achieving scalable quantum photonic technologies, including emission wavelength, deterministic placement, operating temperature, excited-state lifetime, demonstrated pathways toward scalable integration, and reported optical and spin coherence times.

Rare-earth ions, and in particular erbium (Er^{3+}), offer a uniquely compelling platform for quantum photonics by combining telecom-band optical transitions with exceptionally long optical and spin coherence times. Shielding of the 4f electrons gives rise to narrow optical linewidths and optical and spin coherence times extending into the hundreds of microseconds. These properties have enabled state-of-the-art demonstrations, albeit exclusively at cryogenic temperatures. **Table S1** contextualizes the reported coherence properties alongside scalability considerations and operating temperature.

Blueprint for quantum engineering: How Nanofabrication Can Enable Isolation of Single Ions

The blueprint developed to isolate single Er^{3+} ions within the HNP platform (**Supplemental Figures S2 and S3**) rests on three complementary strategies: (1) nanoscale fabrication including geometric confinement via nanostructuring, which limits the physical volume accessible to implanted ions; (2) implantation dose, which independently sets the average ion spacing within that volume; and (3) g^2-based photon correlation measurements, which serve as an experimental calibration for the single-ion regime. Isolation is further supported by an upconversion-mediated PL mapping, which improves PL readout efficiency owing to the faster upconversion excited-state lifetime (164 μs at 520 nm) and enables spatial imaging of individual emitters. **Figure S7** shows a ~3 × 3 μm^2 area of the HNP1 A4 array mapped using this method.

Pillar 1 - geometric confinement

As illustrated in **Figure S2**, transitioning from a bulk or thin-film host matrix to a nanostructured geometry progressively reduces the physical volume accessible to implanted Er ions, directly limiting the number of ions that can reside within a fixed optical excitation beam spot (blue region, **Figure S2**).

Pillar 2 - dose control

Independent of geometry, the average Er ion separation is controlled through the implantation dose (**Figure S2B**). For a dose of 10^{14} cm^{-2}, the concentration is calculated from the SRIM-derived straggle (~20 nm):

$$= \frac{dose}{straggle} = \frac{10^{14}\ cm^{-2}}{20 \times 10^{-7}\ cm^{-1}} = 5 \times 10^{19}\ cm^{-3}$$

yielding an average ion spacing of ~2.7 nm, increasing to ~12.6 nm at a dose of 10^{12} cm^{-2}.

The estimated number of Er ions within a given structure follows from combining geometric confinement and dose. For a single HNP, the area is first calculated from the inner and outer radii:

$$A_{HNP} = \pi(r_o^2 - r_i^2)$$

$$A_{HNP} = 5.5 \times 10^{-12}\ cm^2.$$

For the tunable telecom laser (~1525–1565 nm), the diffraction-limited spot FWHM is ~868 nm, corresponding to ~12 HNPs within the spot. The number of ions per HNP is then N = dose × A_{HNP}, giving ~60 ions for the HNP areas in **Figure S3** at a dose of 10^{12} cm^{-2} (this number can be further tuned by adjusting the encapsulation oxide thickness, which governs the ion range reaching the pillars). The same approach gives ~5 ions for the structure in **Figure S1B**, and the corresponding bulk reference in that figure is implanted at a correspondingly lower dose to match this ion count $N_{ex,bulk} = dose \times \pi r^2$.

For the calibration nanowire structures, the number of excited ions is calculated as:

$$N_{ex,NW} = \frac{NW\ length}{d} \times \frac{straggle}{d}$$

Figure S2C compares the resulting ion counts for bulk and nanostructured geometries as a function of dose within a ~450 nm excitation spot.

Experimental validation of pillars 1 and 2

This geometric and dose-based confinement is validated experimentally. At the high implantation dose used for initial calibration (NW1, 10^{14} cm^{-2}), confocal PL scans reveal dense distributions of bright emission sites consistent with ensemble Er^{3+} emission. As the dose is reduced to 10^{13} and 10^{12} cm^{-2} (NW2, NW3), PL intensity decreases correspondingly, and further reducing the critical dimension to 5 nm at the same dose (NW4, 10^{12} cm^{-2}) produces isolated emission spots consistent with excitation of only a few Er^{3+} ions (**Figure S11**). This trend is corroborated by power-dependent PL (PDPL) measurements: the decrease in saturation intensity with decreasing ion number follows directly from the rate-equation description of a two-level system:

$$\frac{dN^*}{dt} = \sigma\varphi(N_{Er} - N^*) - \frac{N^*}{\tau}$$

where N^* is the excited concentration of Er ions, N_{Er} is the total concentration of Er ions, σ is the effective excitation cross section, τ is the PL lifetime, and φ is the photon flux. Under steady-state excitation

$$\frac{dN^*}{dt} = 0$$

and the PL intensity at saturation, I_{sat} is

$$I_{sat} = \frac{\eta_{sys} N_{Er}}{\tau_r}$$

where η_{sys} is the total system efficiency, and τ_r is the radiative lifetime. Furthermore, the Er intensity can be expressed as a function of photon flux as

$$I = \frac{I_{sat}}{1 + \frac{1}{\sigma \phi \tau}}.$$

This equation is used to model the theoretical power dependence of the Er^{3+} lithium niobate control samples with a small number of ions, as plotted in **Figure S1**. This is calculated considering an excitation cross-section of ~10^{-20} cm^{-2}, [1] and a calculated I_{sat} that is ~16x lower than the HNP sample, considering a η_{sys} 10× lower than that of the NS (due to the decrease in extraction efficiency of the LN sample) and a τ_r = 4.2 ms.

Pillar 3 - g^2 calibration

Figure S14 summarizes $g^2(\tau)$ measurements acquired at multiple spatially distinct spots across the HNP array (HNP1) under varying excitation conditions, providing the third and final pillar of the blueprint: using g^2 as a calibration for the single-ion regime. Measurements were performed primarily at room temperature (296 K), with a representative measurement at 77 K, across excitation wavelengths spanning resonant visible (458 nm), near-infrared (980 nm), and telecom C-band (195.44 THz). **Figure S14** also shows three representative g^2 measurements for spots A2_G, A2_H, and A2_I (identified in the telecom PL intensity map, **Figure S14**), showing a progressive decrease in $g^2(0)$ toward the single-ion regime (0.89, 0.53, and 0.48).

Supplementary measurements on Er qubits

This section provides additional optical characterization supporting the main-text results: validation of single-photon emission at an independent qubit site, the photon-echo methodology used to extract coherence times, and further characterization of the upconversion-based readout scheme.

Figure S8 presents additional optical characterization of one of the additional Er^{3+} qubit sites (Q2). g^2 measurements of the telecom PL yield $g^2(0) = 0.35$, indicating single-photon emission from a single Er^{3+} ion within the excitation volume. PLE measurements using telecom-band detection show emission centered at 195.4 THz, with PLE also confirming upconversion-based

detection at 660 nm. **Figure S8** further shows room-temperature PDPL and time-resolved PL (TRPL) measurements of Q2 under resonant excitation at ~195.44 THz.

Figures S5 and S6 present the two-pulse photon echo measurement sequence ($\pi/2$ - π) and extended data for both 9 and 20 ion measurements shown in Figure 2. The two-pulse sequence relies on the ensemble's macroscopic polarization rephasing to radiate a coherent echo (seen as a photon burst at $t = \tau_{free}$), whose decay in integrated intensity versus τ_{free} gives T_2.

Figure S4 shows upconversion PL images acquired from four different spots on the HNP structure, corresponding to nominally 60, 20, 9, and 1 Er^{3+} ion(s). The PL counts from these images is also used as an estimate for the number of Er ions. The associated uncertainties were calculated through error propagation, accounting for both the uncertainty in the system detection efficiency and the statistical uncertainty of the PL measurements.

Materials science and engineering of SiC_xO_y nanostructured matrix

This section characterizes the structural and optical quality of the SiC_xO_y nanostructured host matrix underlying the platform's coherence and emission properties. **Figure S15** details the CVD growth conditions and growth rate of the SiC_xO_y deposition, as well as related microstructural and morphological characterization (Fourier-transform infrared spectroscopy (FTIR), transmission electron microscopy (TEM), and atomic force microscopy (AFM)).

To assess the impact of nanostructuring on nonradiative recombination kinetics, we examine the temperature dependence of the Er^{3+} excited-state lifetime. TRPL decay traces of Er^{3+} emission from ensemble doped 10 nm C.D. Er:NWs measured at room temperature (RT, red) and 77 K (blue) are shown in **Figure S8 D** under 458 nm excitation. The decays are fit with a biexponential equation,

$$I(t) = Aexp\left(-\frac{t}{\tau_1}\right) + Bexp\left(-\frac{t}{\tau_2}\right)$$

where *I(t)* is the PL intensity, A and B are amplitudes, and τ_1, τ_2 are the extracted lifetimes. The average lifetime is calculated from the equation,

$$\tau = T_1 = \frac{A\tau_1^2 + B\tau_2^2}{A\tau_1 + B\tau_2}$$

The decay lifetimes are identical at both temperatures, yielding the same extracted lifetime within experimental uncertainty (±0.1 ms) of ~2.5 ms, consistent with the indication that nonradiative recombination pathways are suppressed in the nanostructures.

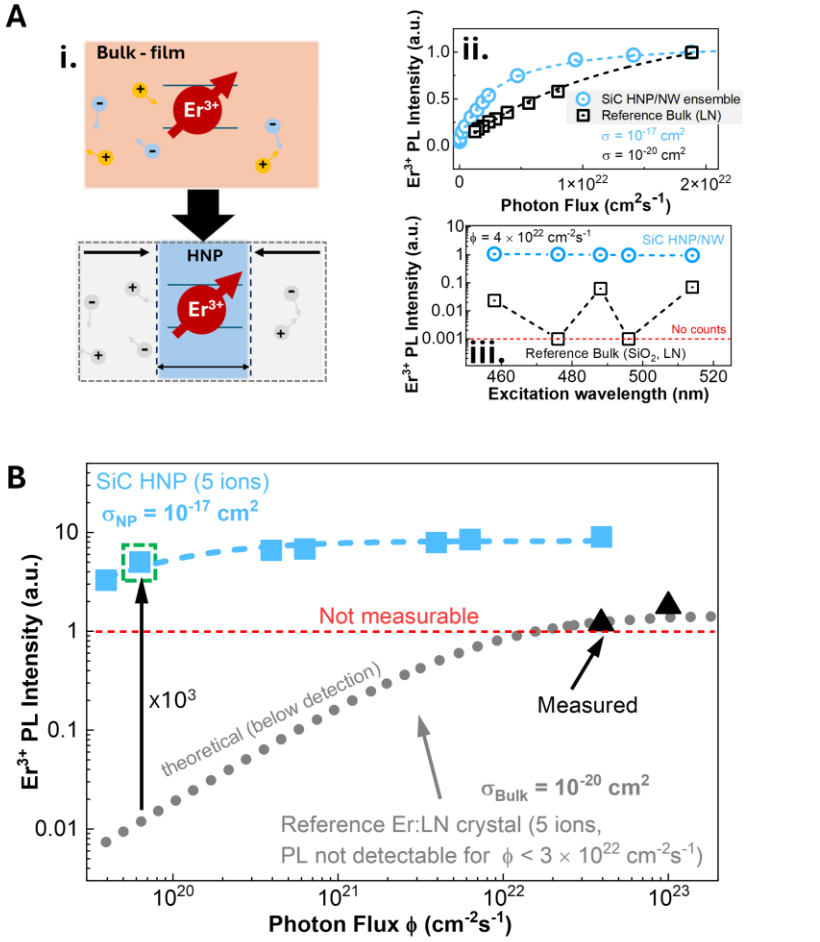


Figure S1: Enhanced excitation cross-section σ, for Er^{3+} in sub-5 nm HNP arrays enabling room-temperature single-Er^{3+}-ion detection. **(A) i.** Schematic illustrating how spatial isolation and nanostructuring of Er^{3+} ions reduces presence of defects, charge fluctuations, and phonon density of states compared to bulk environments. **ii.** Telecom-PDPL studies and fits demonstrate that ensemble Er^{3+} in the HNP/NW has $\sigma \approx 2 \times 10^{-17}$ cm^2, which is 2-3 orders of magnitude higher than typical values in bulk rare-earth hosts; for example, as seen in the Er-implanted LN thin films (reference). **iii.** Broadband excitation behavior of ensemble Er^{3+} in HNP/NW compared to ensemble bulk reference (Er:LN and Er:SiO_2), as demonstrated by PLE at non-resonant (476 nm and 496 nm) excitations while monitoring the telecom emission. **(B)** Representative Er^{3+}-PL from Er:HNP array, containing ~5 Er^{3+}, exhibits an intensity ~3 orders of magnitude higher than the calculated intensity from the reference at the primary photon-flux (φ ~5×10^{19} $cm^{-2}\cdot s^{-1}$) used in the experiments (telecom-resonant excitation ~1533.9 nm). In contrast, the PL in the reference, with an equivalent number of Er ions, remains essentially undetectable even at the highest excitation photon flux used, $\varphi > 9\times10^{22}$ $cm^{-2}\cdot s^{-1}$, a three-order higher value than the primary flux.

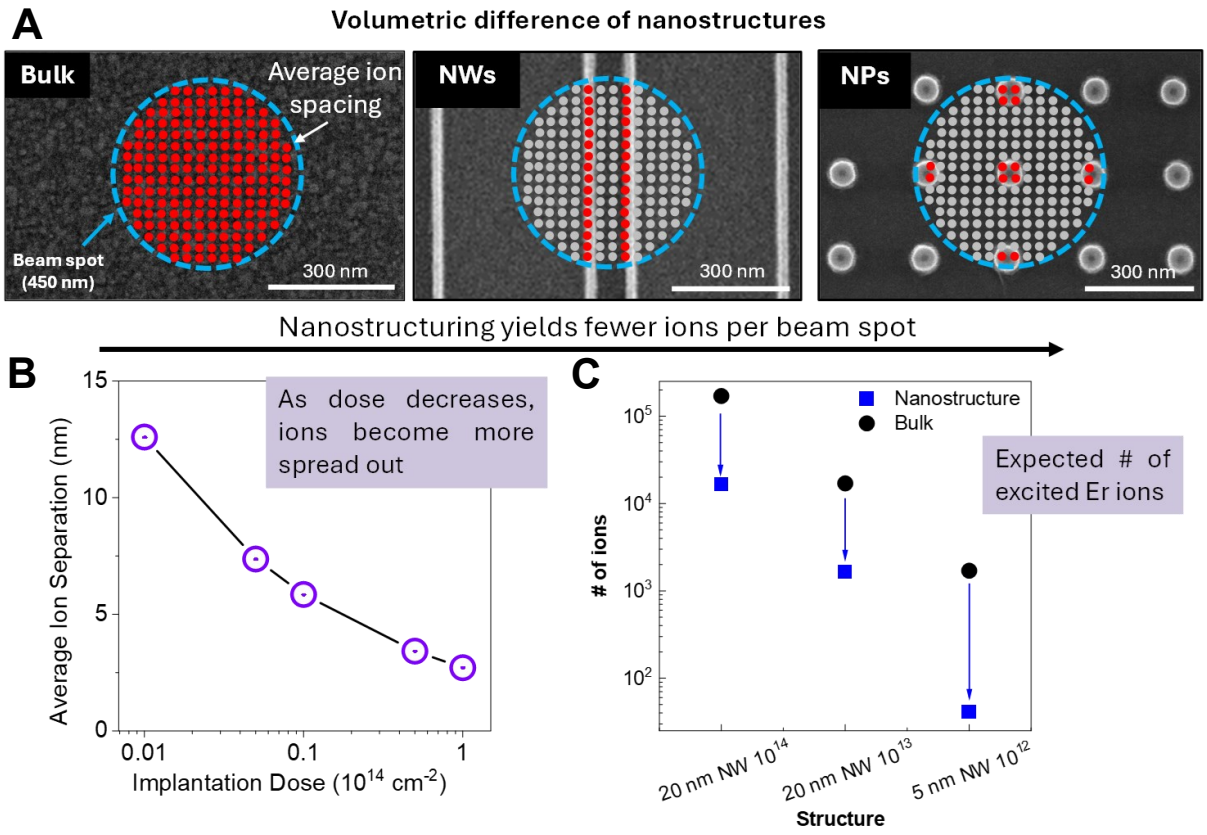
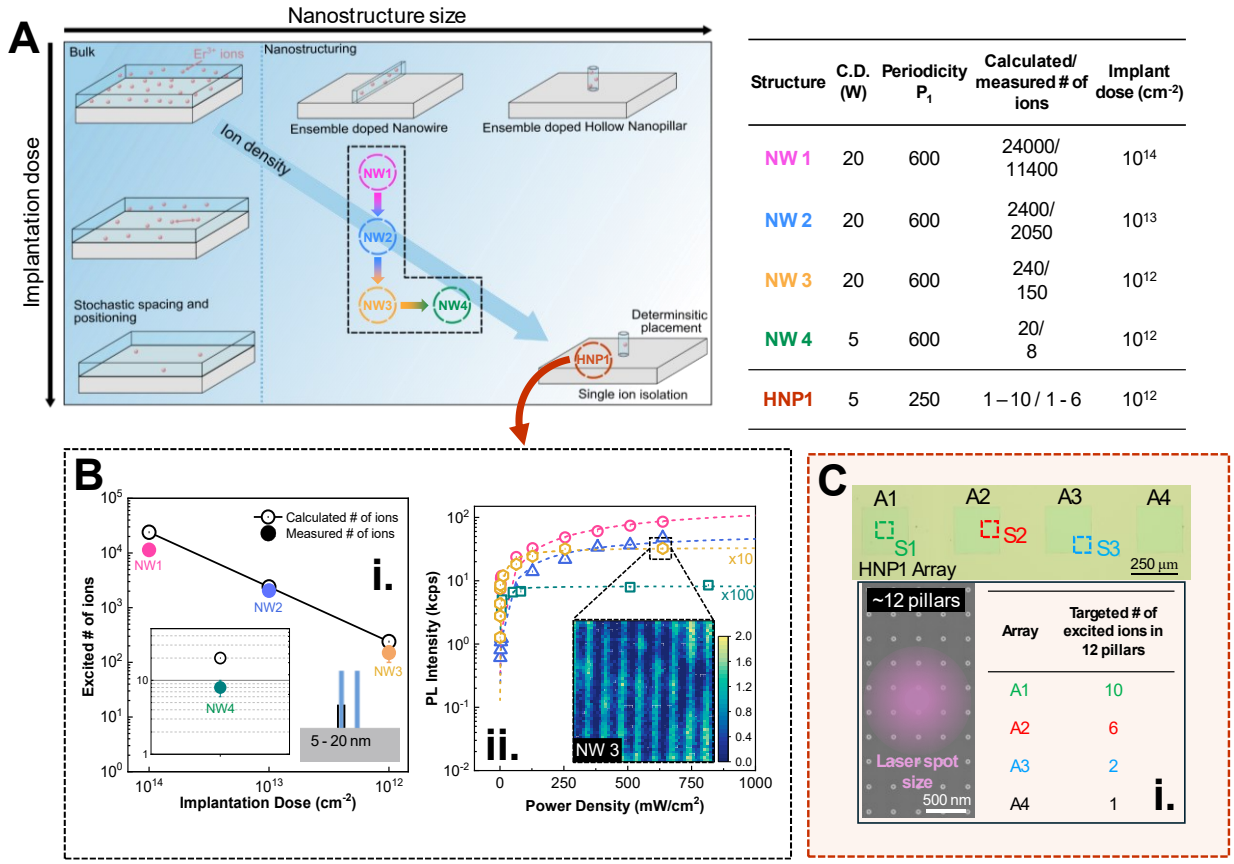


Figure S2: Role of nanostructuring in enabling single-ion isolation. A. Representative SEM images of bulk SiC_xO_y, NW, and HNP geometries overlaid with schematics of the optical excitation volume. Red circles denote Er ions located within the excitation volume, while gray markers indicate ions outside the SiC_xO_y volume. As the host geometry transitions from bulk to progressively confined NSs, the effective excitation volume is reduced, decreasing the number of Er ions excited. **B.** Calculated average Er ion separation as a function of implantation dose, illustrating the increasing spatial separation of ions at lower doses. **C.** Comparison of the calculated number of excited Er ions within a ~450 nm excitation spot for bulk and nanostructured SiC_xO_y as a function of implantation dose and NS C.D. The reduction in the number of excited ions with decreasing structural volume and implantation dose highlights the role of nanostructuring in isolating single Er ions.



Structure	C.D. (W)	Periodicity P_1	Calculated/ measured # of ions	Implant dose (cm^{-2})
NW 1	20	600	24000/ 11400	10^{14}
NW 2	20	600	2400/ 2050	10^{13}
NW 3	20	600	240/ 150	10^{12}
NW 4	5	600	20/ 8	10^{12}
HNP1	5	250	1 – 10 / 1 - 6	10^{12}

Figure S3: Blueprint for spatially-resolved single-ion isolation in HNP arrays. **A.** A combined nanostructuring and implantation strategy enables deterministic isolation of single Er^{3+}. Starting from a bulk/ thin-film SiC_xO_y host with randomly distributed Er ions, HNP geometries confine ions laterally and reduce the effective ion density within the optical excitation volume. By tuning implantation dose (*y*-axis) and C.D. or number of nanostructures (*x*-axis), the system transitions from ensemble excitation to single-ion isolation. Fabricated NW calibration structures NW1-NW4 and HNP1 serve as experimental testbeds, with calculated and validated ion counts summarized in the accompanying Table. **B. i.** Quantitative validation in NW arrays shows strong agreement between predicted and experimentally extracted number of ions. **ii.** PL saturation confirms emitter density reduction: arrays implanted at 10^{14} cm^{-2} yield ~180 kcps, while 10^{12} cm^{-2} arrays exhibit ~0.08 kcps, consistent with excitation of only a few ions. Confocal telecom PL maps illustrate the shift from bright ensemble emission to isolated sites. **C. i.** For HNP arrays, four designs (A1-A4) target 10, 6, 2, and 1 optically-active Er^{3+}-ions within a 3×4 array.

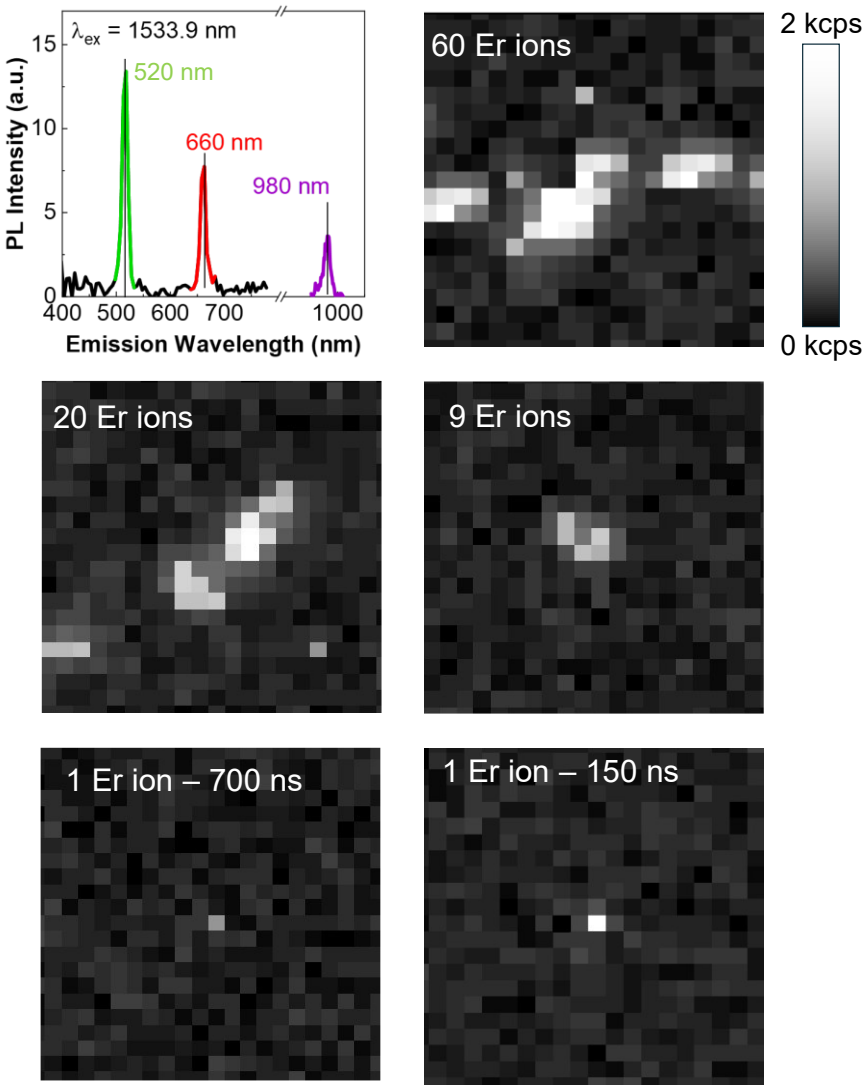


Figure S4: Upconversion imaging of Er ions. Top left shows PL spectra of upconversion emission lines from ensemble of Er^{3+} ions in Er:HNP. Top right and below show upconverted PL images collected at 520 nm from four sites containing approximately 60, 20, 9, and 1 Er ions, respectively. Difference in count rate between two different excitation pulse widths (700 ns and 150 ns) are shown for 1 Er ion.

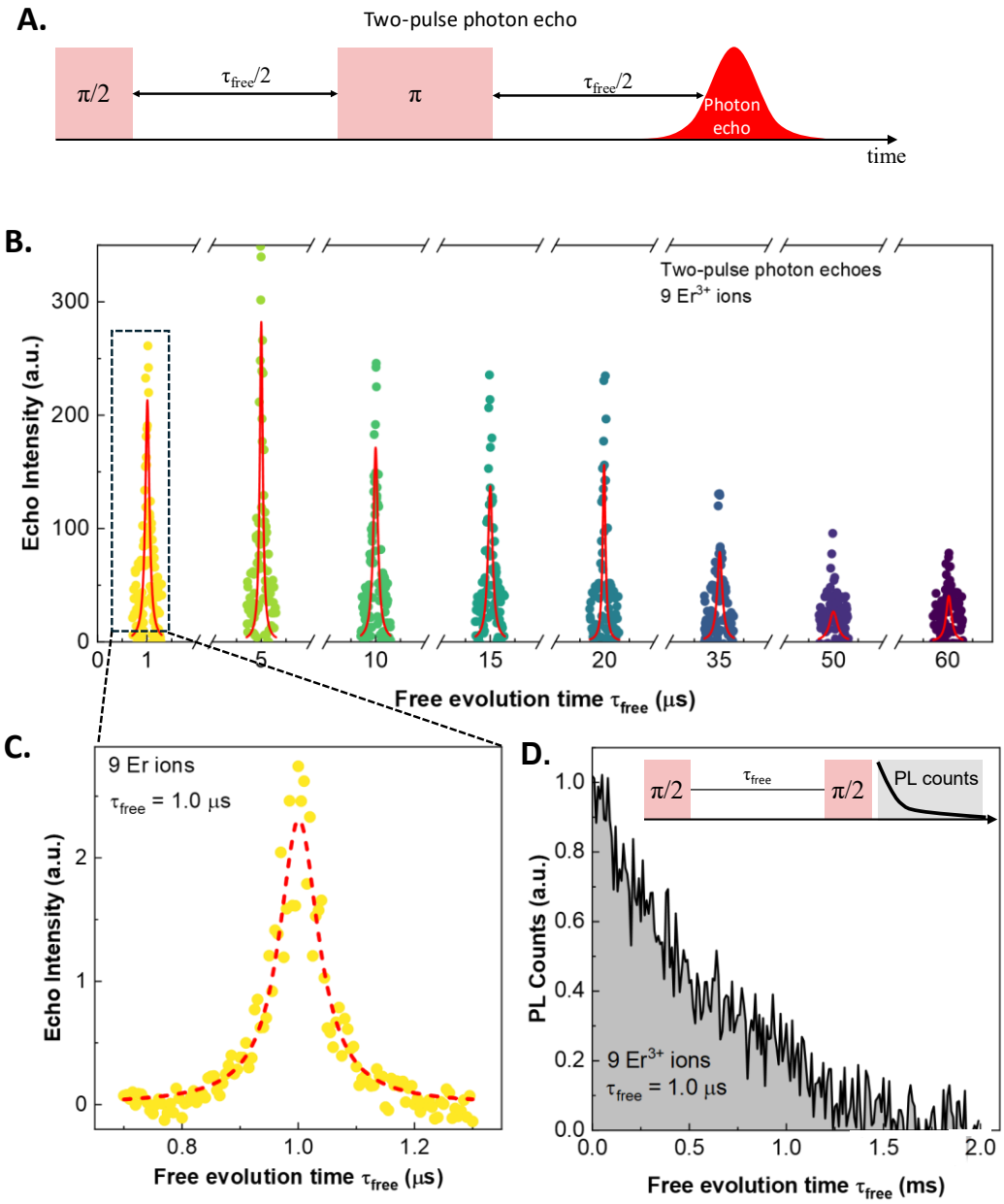


Figure S5: Two pulse photon echoes for 9 ions. A. Schematic of the two-pulse photon echo sequence used to measure T_2 coherence time. **B.** Photon-echo peaks measured at τ_{free} for 9 Er ions using a two-pulse photon echo sequence, with Lorentzian curves to determine integrated intensity. **C.** Corresponding time-resolved telecom emission photon echo from two-pulse photon echo from 9 Er ions for a τ_{free} of 1.0 μs, where the photon echo burst can be seen at 1.0 μs. **D.** Time-resolved telecom photon emission from the Ramsey sequence from 9 Er ions for a τ_{free} of 1.0 μs.

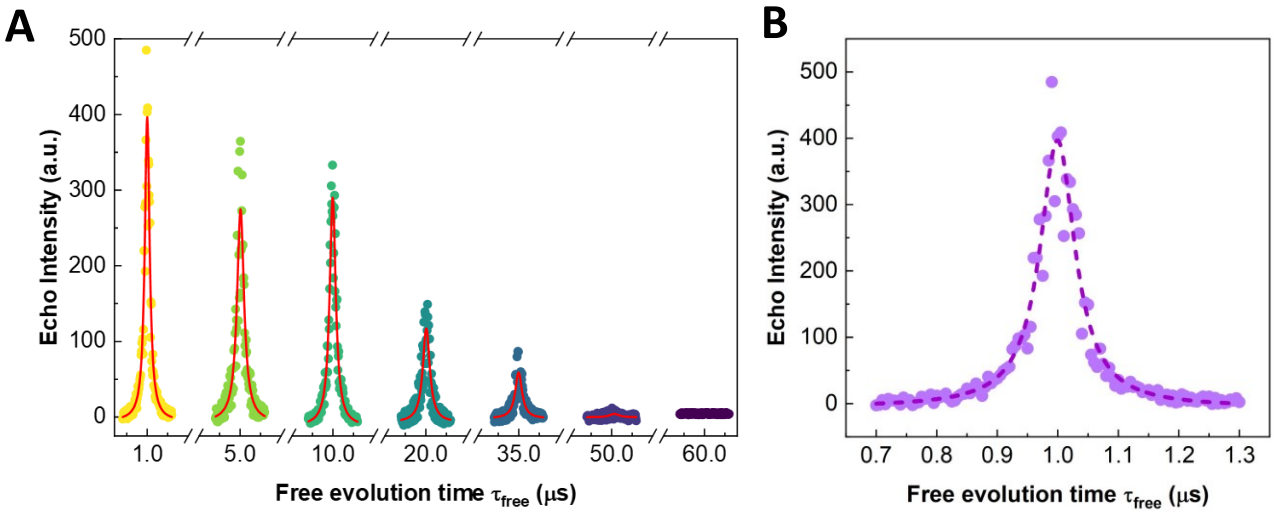


Figure S6: Two pulse echoes for 20 Er ions. A. Time-resolved telecom emission photon echo from two-pulse photon echo from 20 Er ions for a τ_{free} of 1.0, 5.0, 10, 20, 35, 50, and 60 μs. **B.** Zoomed time-resolved telecom emission photon echo from two-pulse photon echo from 20 Er ions for a τ_{free} of 1.0 μs.

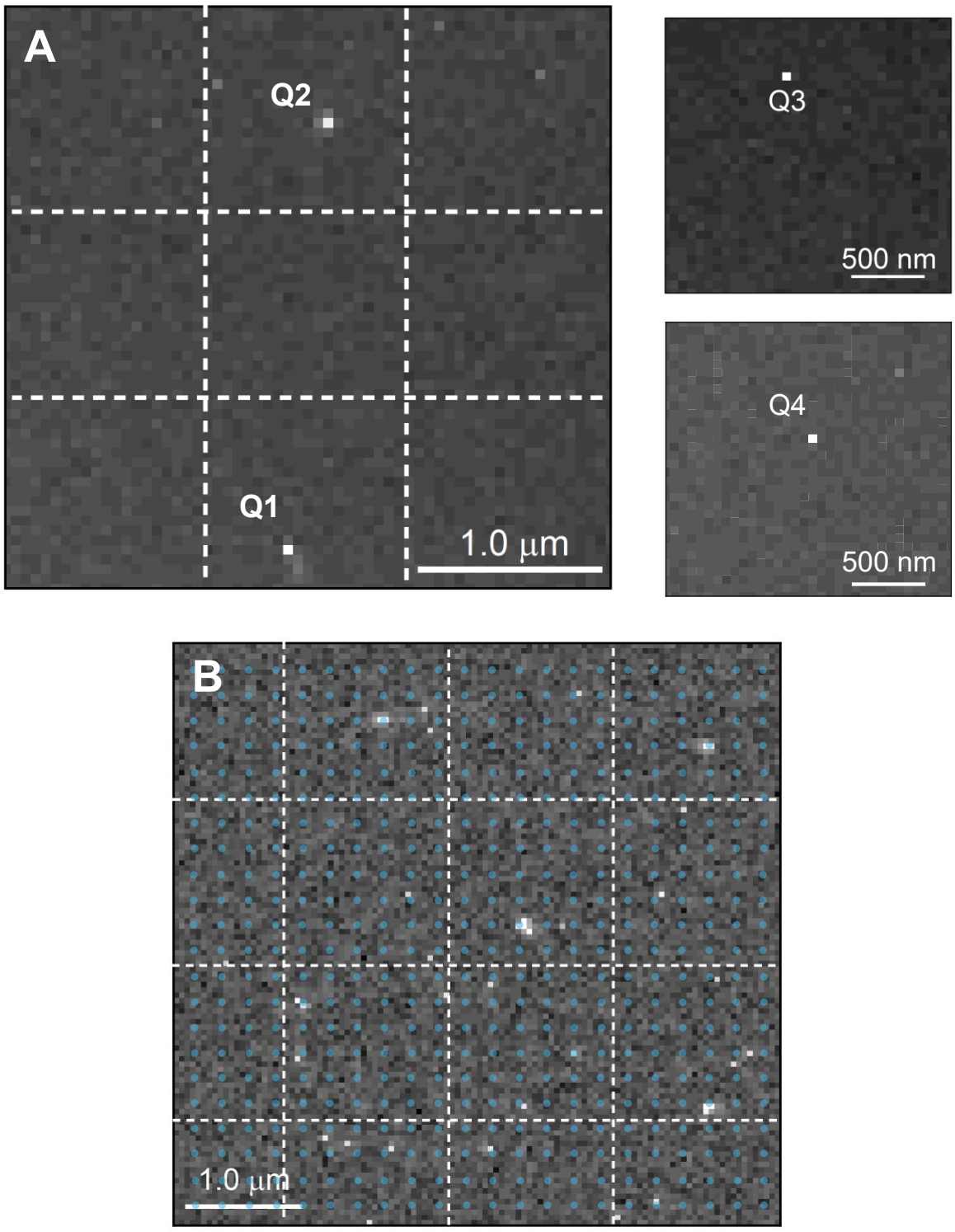


Figure S7: Er^{3+} Upconversion PL imaging. A. PL camera image mappings of 520 nm Er upconversion PL of representative individual spatially isolated Er^{3+} qubits (Q1, Q2, Q3, and Q4) in Er:HNPs (HNP1, array A4). White dashed lines separate HNP array groups based on the $1/e^2$ laser beam diameter. **B.** PL camera image mapping of HNP1 A2, overlayed with positions of the HNP array.

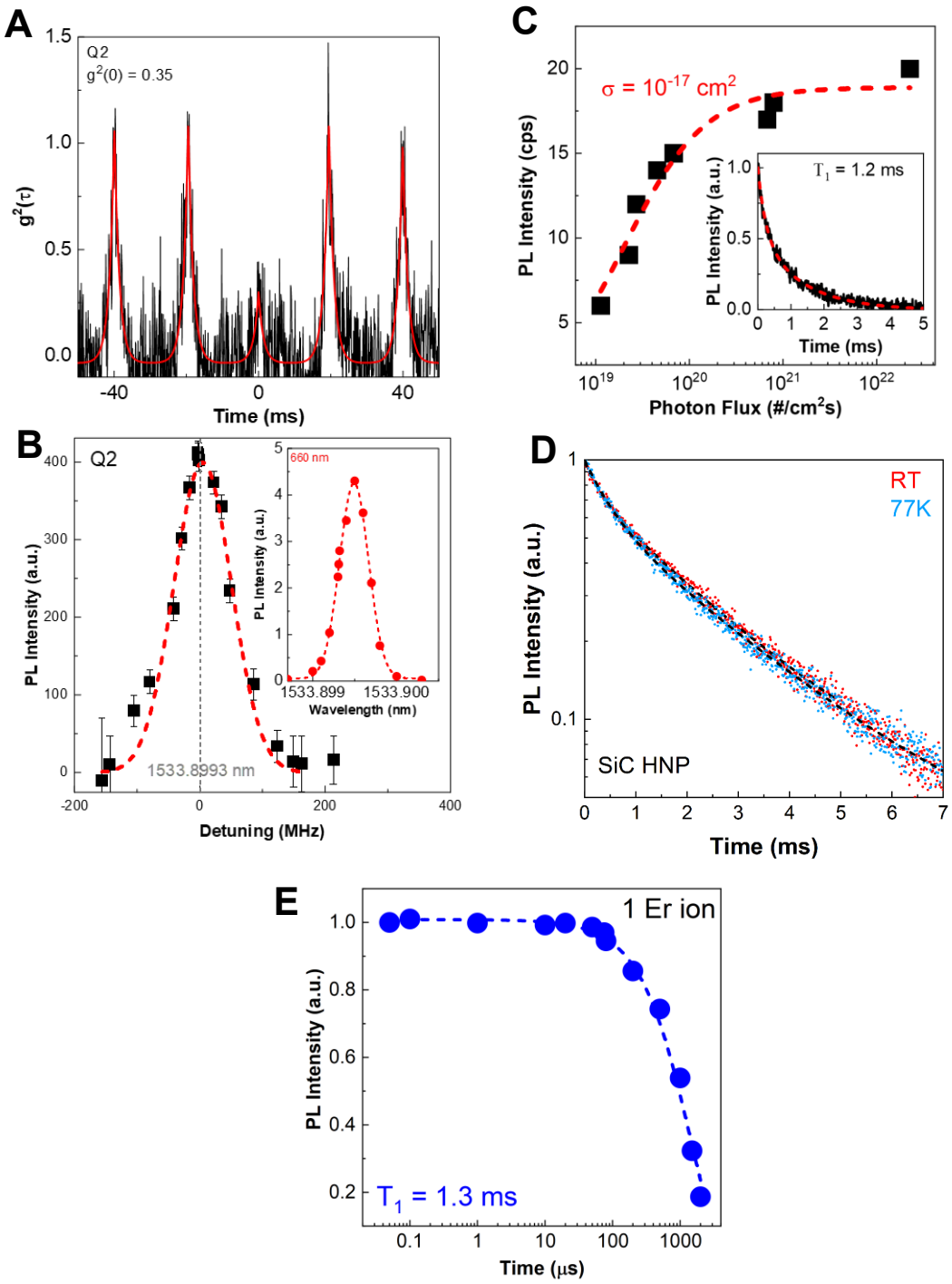


Figure S8: Optical characterization of Er:HNP. A. Room temperature g^2 correlation measurement of qubit Q2 under resonant excitation, yielding a $g^2(0) = 0.35$, confirming single photon emission. **B.** PLE measurements of the telecom and 660 nm upconversion Er emission (inset) of Q2. **C.** PDPL and TRPL measurements of Q2 at room temperature under resonant telecom excitation. **D.** Comparison of TRPL of ensemble Er emission from an ensemble Er:HNP array at RT and 77K under 458 nm excitation. Both decays yield a PL lifetime of ~2.5 ms, independent of temperature. **E.** Measurement of the excited-state lifetime T_1 of a single Er^{3+} ion following resonant excitation with a $\pi/2$ pulse.

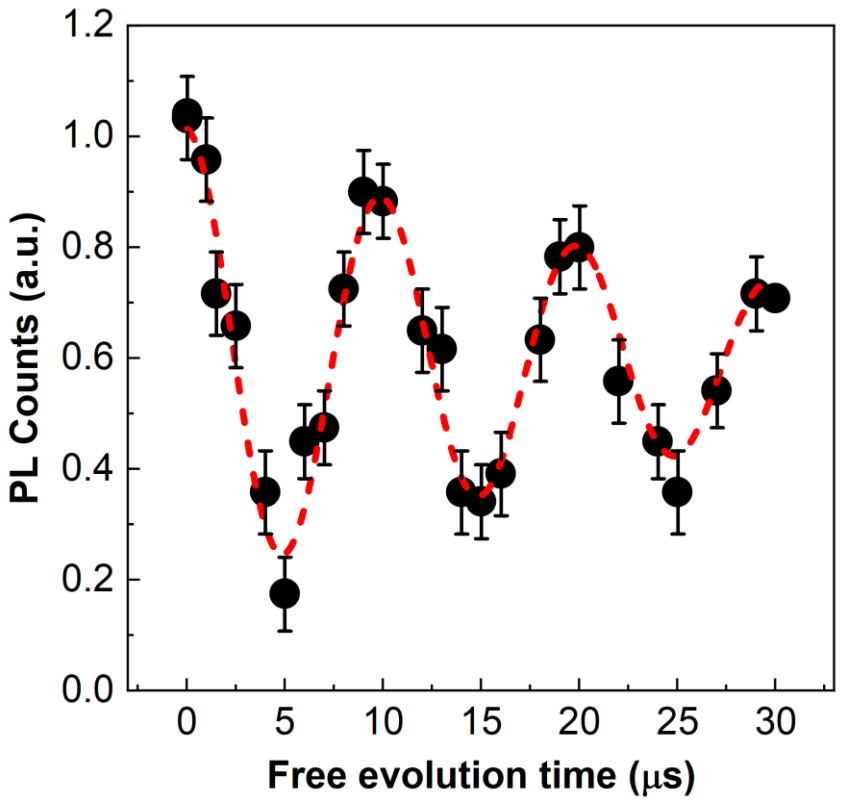


Figure S9: Room temperature Ramsey oscillation measurement of a single Er^{3+} ion under detuned excitation $\Delta f = 0.1$ MHz. Fitting the data to $I_0 + Ae^{\frac{-\tau_{free}}{T_2^*}} \cos(2\pi\Delta f \tau_{free})$ yields an optical coherence time $T_2^* = 29 \pm 4$ μs.

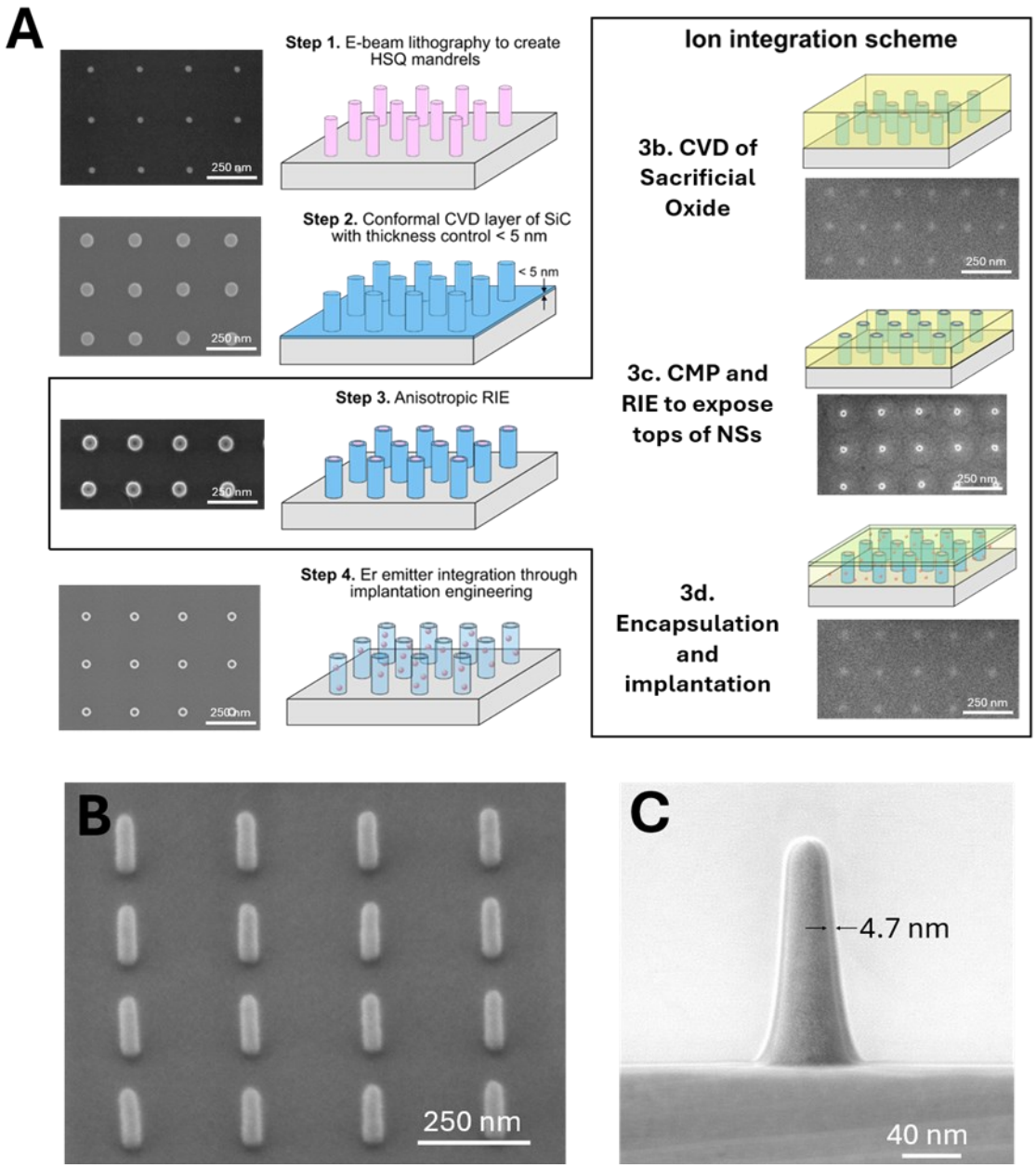


Figure S10: Nanofabrication scheme for Er:HNP arrays. A. Schematic overview of the fabrication sequence used to realize Er:HNPs shown alongside representative top-down SEM images acquired after each major processing step. Steps 1 through 4 illustrate the evolution of the NP (nanopillar) geometry during pattern definition (e-beam lithography), SiC_xO_y deposition, and etching. Step 3 is expanded to explicitly depict the ion-integration process, in which the NP sidewalls serve as lateral implantation apertures to spatially confine Er ions within the engineered SiC_xO_y matrix. **B.** Angled SEM of a NP array**. C.** Cross-section SEM of a HNP after Step 3 showing the HSQ mandrel with a conformal 4.7 nm thick NP sidewall surrounding it.

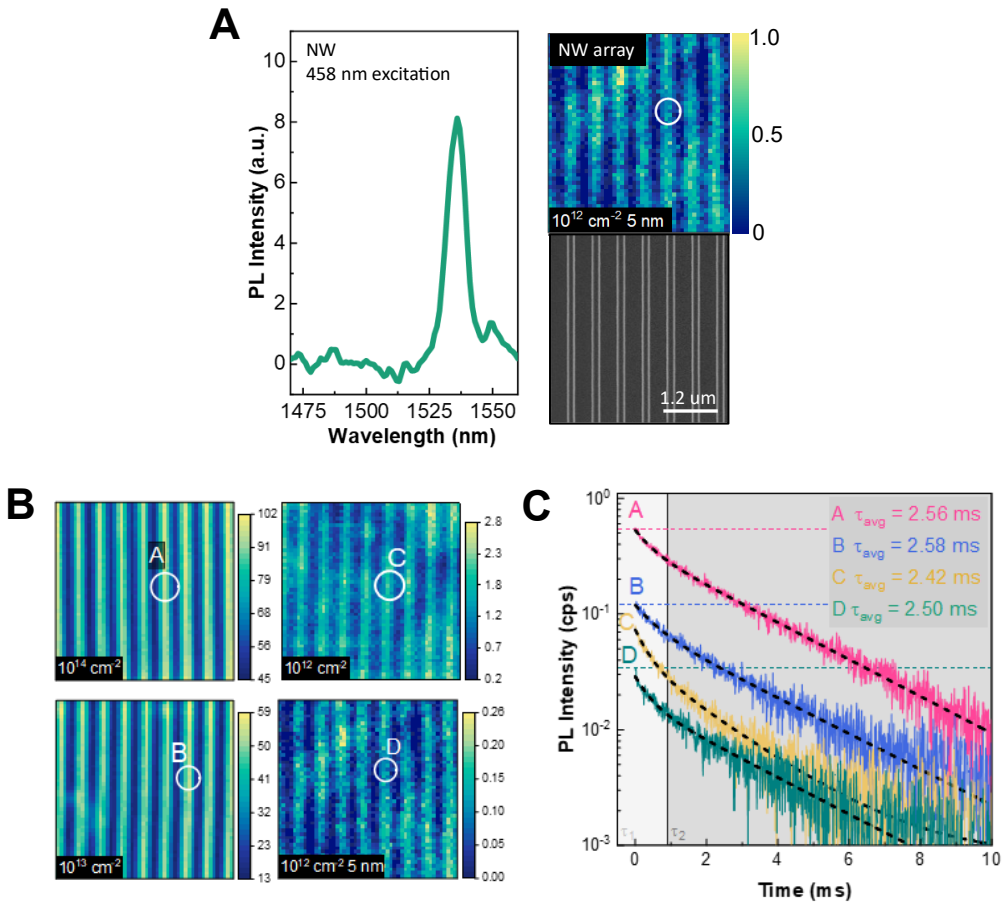


Figure S11: Er^{3+} PL from Er:NW calibration arrays. A. Room-temperature steady-state PL spectrum acquired from an ensemble Er:$SiC_{0.5}O_{1.0}$ NW calibration array implanted at a dose of 10^{12} cm^{-2} under resonant 458 nm excitation. The dominant emission peak is centered at ~1534 nm, corresponding to the Er^{3+} $^4I_{13/2}$ to $^4I_{15/2}$ transition. Inset: confocal PL intensity map (5 × 5 μm²) collected at 1534 nm, showing spatially localized Er emission confined to the NW array region, with no detectable Er-related PL from outside the NWs. Representative top-down SEM image of the corresponding NW array with a C.D. of 5 nm and a pitch of 600 nm. The strong spatial correlation between the PL signal and the NW geometry confirms that the observed Er emission originates from ions incorporated within the nanostructured SiC_xO_y matrix. **B.** Representative confocal steady-state PL maps acquired from four NW arrays (NW1–NW4) implanted with different Er doses, as indicated. White circles mark the locations from which time-resolved measurements were extracted (labeled A–D). The PL contrast reflects spatial variations in Er emission intensity arising from differences in implantation dose and NS geometry. **C.** Corresponding TRPL decay traces measured at the marked locations, shown for Er implantation doses of 10^{14} cm^{-2} (A), 10^{13} cm^{-2} (B), and 10^{12} cm^{-2} (D). Dashed lines indicate biexponential fits used to extract the average excited-state lifetime T_1, yielding comparable values (~2.5–2.6 ms) across all doses and structures.

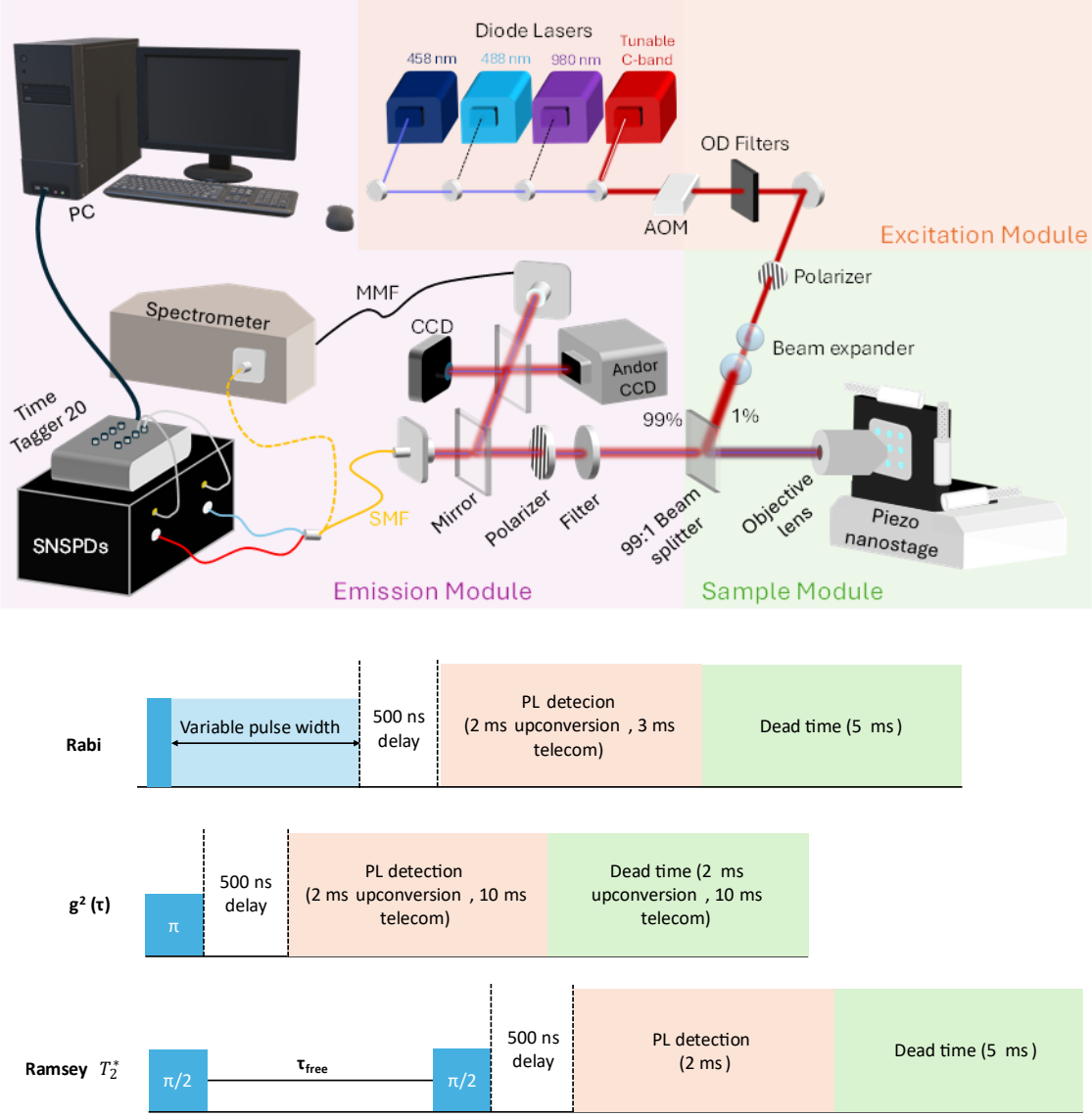


Figure S12: A. Schematic of homebuilt PL microscope and experimental setup. The microscope is divided into three modular sections: the excitation, sample, and emission module, which allows plug/play of different lasers and detectors. The system is enclosed with temperature controllers to control/modulate the ambient temperature of each component. The samples are mounted to a piezo electric nanostage for mapping/positioning. SNSPDs are used for the detection of all PL, which is connected to a Time Tagger 20 for photon counting. **B.** Schematic timing diagrams illustrating the optical pulse and detection sequences employed for Rabi, Ramsey, and g^2 measurements.

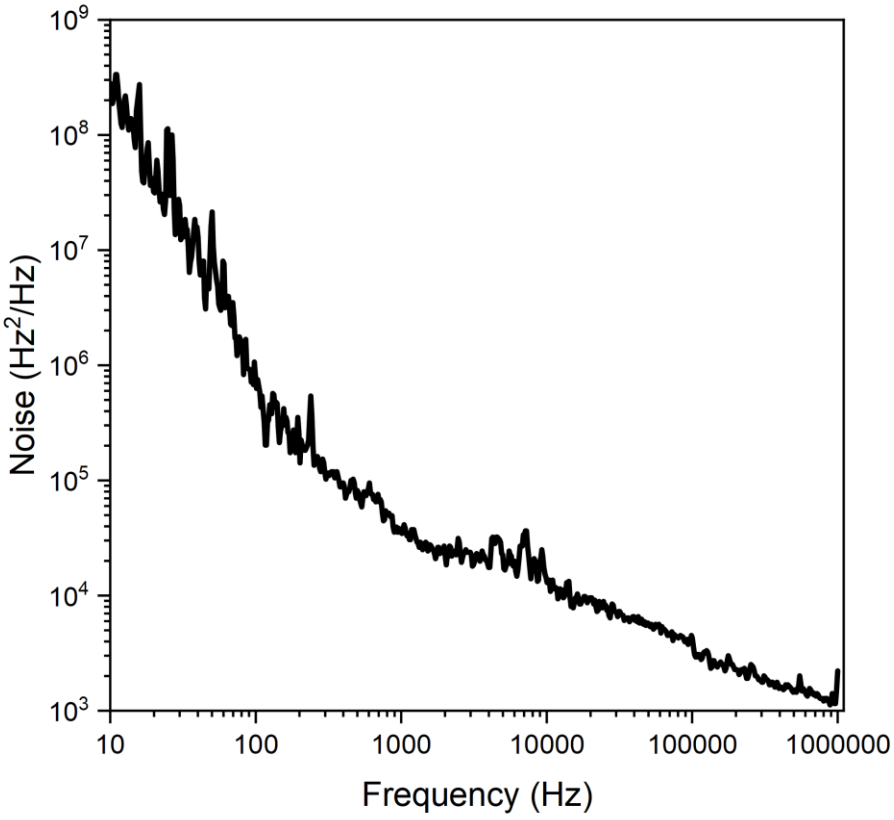
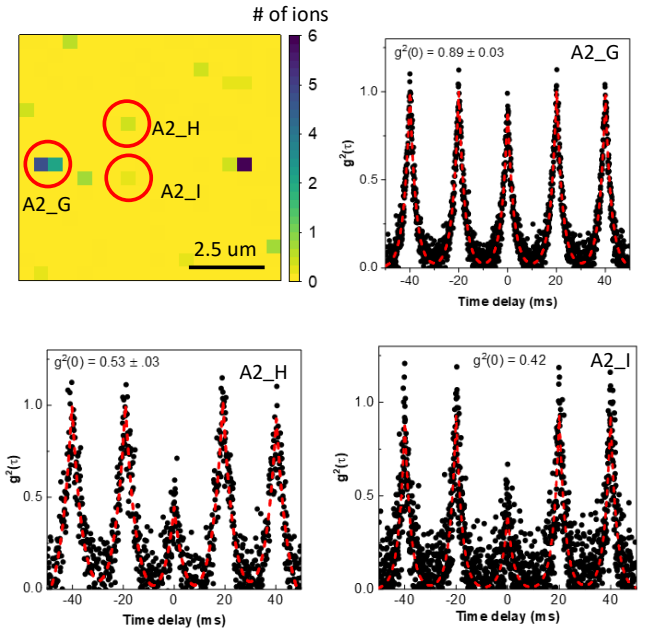


Figure S13: Frequency-modulation noise power spectral density (PSD) measurements of the PPCL550 laser. The Pure Photonics PPCL550 tunable C-band laser has a noise floor of ~1000 Hz^2/Hz, corresponding to a coherence time of ~80 - 100 μs. This decreases to ~32 μs based on the frequencies relevant to the Ramsey and photon-echo pulsing sequences used in this work, as determined using the β-separation-line method. [23] Data provided by Pure Photonics.



HNP1 Site ID	Excitation Wavelength	Temperature (K)	$g^2(0)$	# of ions
A1_A	458 nm	296	0.91 ± 0.02	10
A1_B	458 nm	296	0.90 ± 0.02	10
A1_B	980 nm	296	0.87 ± 0.02	9 - 10
A1_C	458 nm	296	1.00 ± 0.01	>10
A1_C	980 nm	296	1.00 ± 0.01	>10
A1_D	458 nm	296	--	--
A1_E	458 nm	296	1.00 ± 0.01	>10
A2_F	458 nm	296	0.89 ± 0.02	9 - 10
A2_F	1533.9 nm	296	0.80 ± 0.02	5
A2_G	1533.9 nm	296	0.89 ± 0.03	9
A2_H	458 nm	296	0.53 ± 0.03	2 - 3
A2_I	1533.9 nm	77	0.48 ± 0.04	1 - 2

Figure S14: Extended g^2 correlation measurements validating the single-ion isolation blueprint in Er-doped HNPs. The table summarizes second-order intensity correlation measurements acquired from multiple HNP sites (HNP1, A1 and A2), labeled according to the arrays defined in the main manuscript (Figure 1). Measurements were performed under systematically varied excitation conditions, including excitation wavelength, photon flux, excitation pulse width (Δt), and temperature. The extracted $g^2(0)$ values, obtained from fits to the zero-delay peak, provide a quantitative measure of the effective number of optically excited Er^{3+} ions at each site. Representative pulsed $g^2(\tau)$ histograms are shown for three sites (A2_G, A2_H, A2_I), shown in the telecom PL intensity mapping of a 10 x 10 um^2 area at the 195.44 THz Er emission frequency.

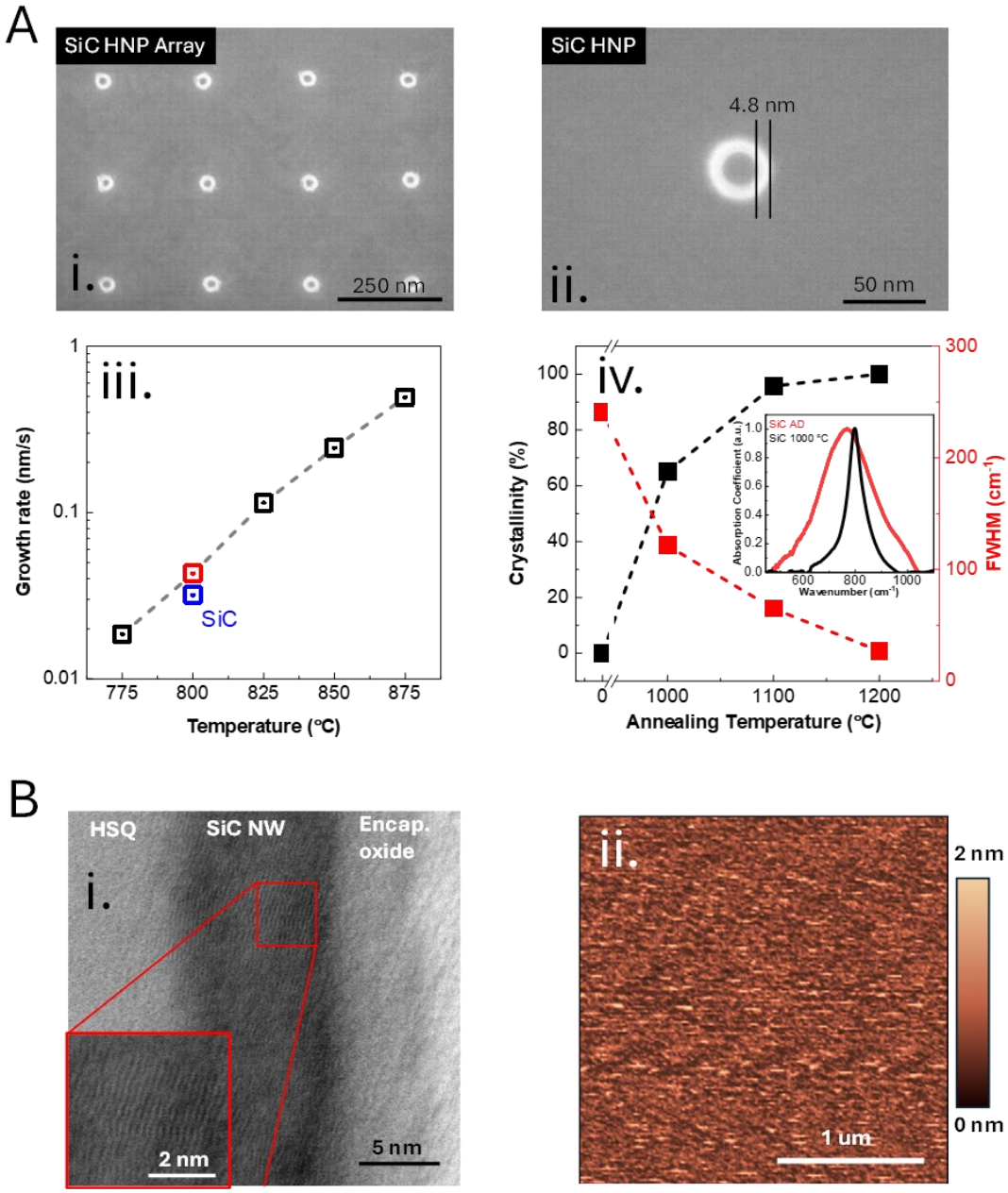


Figure S15: SiC_xO_y HNP growth. A. i. Top-down SEM of a SiC_xO_y HNP array. **ii.** High-magnification top-down SEM of a single 4.8 nm C.D. HNP **iii.** CVD growth rate as a function of deposition temperature. Deposition temperature used in this study is shown in red. Growth rate for stoichiometric a-SiC at 800°C is shown by the blue square. **iv.** Crystallinity percentage (C%) of annealed films as a function of annealing temperature, as determined by deconvolution of the FTIR spectra into Gaussian (G) and Lorentzian (L) components, where C% = 100L/L+G. [2] Inset: Representative FTIR absorption spectra of a 20 nm as-deposited and 900°C annealed stoichiometric SiC film. **B. i.** High-resolution TEM cross-section image of a 10 nm SiC NW sidewall showing crystalline nanodomains. Inset: Magnified TEM image of a SiC crystal domain. **ii.** Representative AFM image of a 10 nm SiC thin film with an RMS roughness value of ~2 Å.

Table S1. SotA NIR and telecom SPE and qubit platforms							
Material systems	**Wavelength (nm)**	**Targeted creation of SPEs**	**Operation temperature†**	**Lifetime (us)**	**Scalable integration§**	**Coherence time T_2^* (μs)**	**Coherence time T_2 (μs)**
SiC							
VV (4H) [3, 4]	~1035 - 1130	Implantation, stochastic	Ambient, 296 K	13.4×10^{-3}	All: SiC Scalability enabled by mature wafer-scale fabrication	0.463 (spin)	23.2 (spin)
			5 K	14.7×10^{-3}		--	Up to 1000 (spin), charge depletion under 270 V
NV (4H) [5]	1176 - 1240	70 ± 10 nm dictated by PMMA mask during nitrogen implantation	Ambient, 296 K	2.1×10^{-3}		--	17.1 (spin)
V^{4+} (4H) [6]	1278(h), 1335(k)	Implantation, stochastic	3.3 K	167×10^{-3}, 45 $\times 10^{-3}$		Unmeasurable due to thermal dephasing at 3.3 K	
Divacancy (3C) [7]	1080 - 1265	Intrinsic, stochastic	20 K	18.7×10^{-3}		1.8 (spin)	901 (spin)
GaN							
Unknown [8]	1085 - 1340	Intrinsic or Mg-doping, stochastic	Ambient, 296 K	0.736×10^{-3}	--	--	--
Si							
G-center/ W-center [9, 10]	1278 /1218	G, W-centers: Implantation, <100 nm resolution using focused ion beam [22]	10 K	32.8 / 7.1× 10^{-3}	Silicon CMOS compatible	--	--
Unknown emitters [11]	1253 – 1448	Origin unknown, stochastic	10 K	4.4 – 30.6 × 10^{-3}	Silicon CMOS compatible	--	--
CNT							
sp^3 defect [12]	1140 - 1580	Stochastic	5 K	--	--	1.2, up to 8.2 with dynamic decoupling (spin)	--
QDs							
InAs/InP [13, 14]	~1529	Stochastic deposition	8.5 K	~1.77× 10^{-3}	Compatible with on-chip integrated detection	--	1058×10^{-6}
Er^{3+}							
TiO_2 [15]	1532.8	Stochastic	0.01 K	2.8×10^3	Integrated on foundry nanophotonic platforms	--	64 (optical)
Si [16]	~1520 - 1550	Implantation, stochastic	0.02 – 0.3 K	345 - 365	Silicon CMOS compatible	--	780 – 1190 (spin)
$LiNbO_3$ [17]	1532	Stochastic	0.02 K	--	Integrated on LNOI photonics platform	--	180 (optical)
$CaWO_4$ [18]	1532	Implantation, stochastic	0.47 K	7.4	--	0.247 (spin)	18 (optical), 44 (spin), >200 (with dynamic decoupling)
$Er(hfac)_4$ [19]	1529	--	10 K	8.66	--	--	0.390 (spin)
Y_2SiO_5 [20]	1538	Stochastic	1.4 K	--	--	--	1 under 0 field. (>1 second under 7 T magnetic field, spin)
CeO_2 [21]	1511-1530	Stochastic	3.2 K	1.04	--	--	0.776 (spin)
HNP (this work)	1534	5 nm as determined by nanostructure C.D. during fabrication	Ambient, 296 K	164 (520 nm upconverted readout), 1.2×10^3 (1534 nm)	CMOS compatible fabrication, self-aligned arrays	32 (optical)	>60 few-ion sites (optical)

§Requires high-yield, efficient, deterministic, and large-scale processing and integration of qubits into PICs.
-- Not demonstrated/addressed
† Under vacuum conditions unless specifically noted

Table S2. Comparison of excited-state lifetime between TRPL and g^2 measurements

Measurement/ Spot (emission wavelength)	**T_1 (ms) from TRPL**	**τ_{PL} (ms) from g^2**
Q1 (1534 nm)	1.2	1.2
Q1 (520 nm)	0.2	0.2
Q1 (980 nm)	0.7	0.6
Q4 (1534 nm)	1.2	1.4
A2 (1534 nm)	2.5	2.6
A3 (1534 nm)	1.6	1.5

References

1. A. Kaloyeros, S. Dutta, S. Gallis, Engineering and polarization properties of erbium-implanted lithium niobate films for integrated quantum applications. APL Materials 12, 071101 (2024).

2. N. Tabassum, M. Kotha, V. Kaushik, B. Ford, S. Dey, E. Crawford, V. Nikas, S. Gallis, On-Demand CMOS-Compatible Fabrication of Ultrathin Self-Aligned SiC Nanowire Arrays. Nanomaterials 8, 906 (2018).

3. Q. Li, J.-F. Wang, F.-F. Yan, J.-Y. Zhou, H.-F. Wang, H. Liu, L.-P. Guo, X. Zhou, A. Gali, Z.-H. Liu, Z.-Q. Wang, K. Sun, G.-P. Guo, J.-S. Tang, H. Li, L.-X. You, J.-S. Xu, C.-F. Li, G.-C. Guo, Room-temperature coherent manipulation of single-spin qubits in silicon carbide with a high readout contrast. National Science Review 9, nwab122 (2022).

4. C. P. Anderson, A. Bourassa, K. C. Miao, G. Wolfowicz, P. J. Mintun, A. L. Crook, H. Abe, J. Ul Hassan, N. T. Son, T. Ohshima, D. D. Awschalom, Electrical and optical control of single spins integrated in scalable semiconductor devices. Science 366, 1225-1230 (2019).

5. J.-F. Wang, F.-F. Yan, Q. Li, Z.-H. Liu, H. Liu, G.-P. Guo, L.-P. Guo, X. Zhou, J.-M. Cui, J. Wang, Z.-Q. Zhou, X.-Y. Xu, J.-S. Xu, C.-F. Li, G.-C. Guo, Coherent Control of Nitrogen-Vacancy Center Spins in Silicon Carbide at Room Temperature. Physical Review Letters 124, 223601 (2020).

6. G. Wolfowicz, C. P. Anderson, B. Diler, O. G. Poluektov, F. J. Heremans, D. D. Awschalom, Vanadium spin qubits as telecom quantum emitters in silicon carbide. Science Advances 6, eaaz1192 (2020).

7. D. J. Christle, P. V. Klimov, C. F. de las Casas, K. Szász, V. Ivády, V. Jokubavicius, J. U. Hassan, M. Syväjärvi, W. F. Koehl, T. Ohshima, N. T. Son, E. Janzén, Á. Gali, D. D. Awschalom, Isolated Spin Qubits in SiC with a High-Fidelity Infrared Spin-to-Photon Interface. Physical Review X 7, 021046 (2017).

8. Y. Zhou, Z. Wang, A. Rasmita, S. Kim, A. Berhane, Z. Bodrog, G. Adamo, A. Gali, I. Aharonovich, W. Gao, Room temperature solid-state quantum emitters in the telecom range. Science Advances 4, eaar3580 (2018).

9. W. Redjem, A. Durand, T. Herzig, A. Benali, S. Pezzagna, J. Meijer, A. Yu. Kuznetsov, H. S. Nguyen, S. Cueff, J.-M. Gérard, I. Robert-Philip, B. Gil, D. Caliste, P. Pochet, M. Abbarchi, V. Jacques, A. Dréau, G. Cassabois, Single artificial atoms in silicon emitting at telecom wavelengths. Nature Electronics 3, 738-743 (2020).

10. Y. Baron, A. Durand, P. Udvarhelyi, T. Herzig, M. Khoury, S. Pezzagna, J. Meijer, I. Robert-Philip, M. Abbarchi, J.-M. Hartmann, V. Mazzocchi, J.-M. Gérard, A. Gali, V. Jacques, G. Cassabois, A. Dréau, Detection of Single W-Centers in Silicon. ACS Photonics 9, 2337-2345 (2022).

11. A. Durand, Y. Baron, W. Redjem, T. Herzig, A. Benali, S. Pezzagna, J. Meijer, A. Yu. Kuznetsov, J.-M. Gérard, I. Robert-Philip, M. Abbarchi, V. Jacques, G. Cassabois, A. Dréau, Broad Diversity of Near-Infrared Single-Photon Emitters in Silicon. Physical Review Letters 126, 083602 (2021).

12. J.-S. Chen, K. J. Trerayapiwat, L. Sun, M. D. Krzyaniak, M. R. Wasielewski, T. Rajh, S. Sharifzadeh, X. Ma, Long-lived electronic spin qubits in single-walled carbon nanotubes. Nature Communications 14, 848 (2023).

13. M. Anderson, T. Müller, J. Huwer, J. Skiba-Szymanska, A. B. Krysa, R. M. Stevenson, J. Heffernan, D. A. Ritchie, A. J. Shields, Quantum teleportation using highly coherent emission from telecom C-band quantum dots. npj Quantum Information 6, 14 (2020).

14. K. D. Zeuner, M. Paul, T. Lettner, C. Reuterskiöld Hedlund, L. Schweickert, S. Steinhauer, L. Yang, J. Zichi, M. Hammar, K. D. Jöns, V. Zwiller, A stable wavelength-tunable triggered source of single photons and cascaded photon pairs at the telecom C-band. Applied Physics Letters 112, 173102 (2018).

15. S. Gupta, R. M. Pettit, A. Sundaresh, V. Niaouris, S. Deckoff-Jones, D. P. Crowley, L. G. Carpenter, A. M. Dibos, M. K. Singh, S. E. Sullivan, Erbium quantum memory platform with long optical coherence via back-end-of-line deposition on foundry-fabricated photonics. Physical Review Applied 24, 054037 (2025).

16. I. R. Berkman, A. Lyasota, G. G. de Boo, J. G. Bartholomew, S. Q. Lim, B. C. Johnson, J. C. McCallum, B.-B. Xu, S. Xie, N. V. Abrosimov, H.-J. Pohl, R. L. Ahlefeldt, M. J. Sellars, C. Yin, S. Rogge, Long optical and electron spin coherence times for erbium ions in silicon. npj Quantum Information 11, 66 (2025).

17. S. Wang, L. Yang, M. Shen, W. Fu, Y. Xu, R. L. Cone, C. W. Thiel, H. X. Tang, Er:LiNbO3 with High Optical Coherence Enabling Optical Thickness Control. Physical Review Applied 18, 014069 (2022).

18. S. Ourari, Ł. Dusanowski, S. P. Horvath, M. T. Uysal, C. M. Phenicie, P. Stevenson, M. Raha, S. Chen, R. J. Cava, N. P. de Leon, J. D. Thompson, Indistinguishable telecom band photons from a single Er ion in the solid state. Nature 620, 977-981 (2023).

19. L. R. Weiss, G. T. Smith, R. A. Murphy, B. Golesorkhi, J. A. Méndez Méndez, P. Patel, J. Niklas, O. G. Poluektov, J. R. Long, D. D. Awschalom, A high-resolution molecular spin-photon interface at telecommunication wavelengths. Science 390, 76-81 (2025).

20. M. Rančić, M. Hedges, R. Ahlefeldt, M. Sellars, Coherence time of over a second in a telecom-compatible quantum memory storage material. Nature Physics 14, 50-54 (2018).

21. Wong, J. et al. Coherent erbium spin defects in colloidal nanocrystal hosts. ACS Nano 18, 19110–19123 (2024).

22. Hollenbach, M. et al. Wafer-scale nanofabrication of telecom single-photon emitters in silicon. Nature Communications 13, 7586 (2022).

23. G. Di Domenico, S. Schilt, P. Thomann, Simple approach to the relation between laser frequency noise and laser line shape. Applied Optics 49, 4801-4807 (2010).